ARMA 20–1237

Third-order elastic tensor of shales determined through ultrasonic velocity measurements

Duda, M.I. and Holt, R.M.
Norwegian University of Science and Technology, Trondheim, Norway
Bakk, A.
SINTEF Industry, Department of Petroleum, Trondheim, Norway

This paper was prepared for presentation at the 54th US Rock Mechanics/Geomechanics Symposium held in Golden, Colorado, USA, 28 June-1 July 2020. This paper was selected for presentation at the symposium by an ARMA Technical Program Committee based on a technical and critical review of the paper by a minimum of two technical reviewers. The material, as presented, does not necessarily reflect any position of ARMA, its officers, or members.

ABSTRACT: Static and dynamic behavior of isotropic or anisotropic media, including rocks, are conveniently described with a second-order stiffness matrix using the Voigt notation, which linearly relates stress changes to strains. However, experimental and field observations indicate that the dynamic stiffness of rocks is stress dependent. We investigate a model proposed by Fuck and Tsvankin employing a constitutive third-order elastic tensor to describe the non-linear strain sensitivity of the stiffness. By using laboratory measurements of strains and ultrasonic P- and S-wave velocities in multiple directions, we were able to invert for all the third-order parameters. We used the third-order elastic tensor to model changes in ultrasonic velocities and investigated the impact of different third-order tensor component optimization schemes on the accuracy of the velocity estimates. To our knowledge this is the first fit of dynamic stiffness of a shale to a third order constitutive model that is not restricted to isotropic strain sensitivity.

1. INTRODUCTION

Elastic properties of most of the earth crust rocks are direction-dependent (e.g. Thomsen, 1986), which makes anisotropy an important factor for rock stiffness and seismic wave velocity analysis. The static and dynamic properties of an anisotropic medium are usually represented by a second-order elastic (SOE) matrix C_{ij}, which linearly relates stress changes with corresponding strains (Fjær et al., 2008).

However, experimental and field data suggest that the dynamic stiffness of rocks is stress-dependent (e.g. Johnson and Rasolofosaon, 1996), i.e. the relationship between stress and deformation is non-linear. This behavior can be described in terms of stiffening grain contacts (Bachrach and Avseth, 2008; Mindlin, 1949; Walton, 1987) or with the use of crack-based models (Budiansky and O'Connell, 1976; Fjaer, 2006; Hudson, 1981). Alternatively, we can use higher order constitutive models (e.g. Prioul et al., 2004), which until now have not been systematically investigated for sedimentary rocks.

Our aim was to derive a third-order elastic (TOE) tensor c_{ijk} which we could use to approximate the dynamic behavior of transversely isotropic shales under different stress state development scenarios and verify it using laboratory data collected on shale samples. This approach is based on a fully physical strain-dependent third-order constitutive model for which we assume vertical transverse isotropy (VTI, i.e. the symmetry axis normal to the plane of isotropy) of stiffnesses and the applied stresses, which allowed us to limit the number of model parameters. Contrary to previous studies (Fuck et al., 2009; Johnson and Rasolofosaon, 1996; Prioul et al., 2004), we do not assume isotropic strain sensitivity of the velocities, which may seem to be an over-simplification for inherently anisotropic materials like shales. Velocity changes are measured in multiple directions for different stress changes. These data are used to determine the elastic parameters of two different non-linear models and to evaluate their performance.

2. THEORETICAL BACKGROUND

The starting point for our model is the TOE tensor proposed by Fuck and Tsvankin, 2009. The relationship between changes in stiffness and changes in strains for a VTI medium, where the anisotropy symmetry axis coincides with the axial loading direction, becomes:

$$C_{ij} = C_{ij}^0 + \Delta C_{ij} = C_{ij}^0 + c_{ijk}\Delta\varepsilon_k, \quad (1)$$

where C_{ij}^0 is the stiffness measured at the in-situ stress.

Due to Voigt's notation $c_{ijk} = c_{ikj} = c_{kij} = c_{jik} = c_{jki} = c_{kji}$. For the general (triclinic) case, the distinct VTI components become:

$$\begin{aligned}
C_{11} &= C_{11}^0 + c_{111}\Delta\varepsilon_1 + c_{112}\Delta\varepsilon_2 + c_{113}\Delta\varepsilon_3 \\
C_{12} &= C_{12}^0 + c_{112}\Delta\varepsilon_1 + c_{122}\Delta\varepsilon_2 + c_{123}\Delta\varepsilon_3 \\
C_{13} &= C_{13}^0 + c_{113}\Delta\varepsilon_1 + c_{123}\Delta\varepsilon_2 + c_{133}\Delta\varepsilon_3 \\
C_{22} &= C_{22}^0 + c_{122}\Delta\varepsilon_1 + c_{222}\Delta\varepsilon_2 + c_{223}\Delta\varepsilon_3 \\
C_{23} &= C_{23}^0 + c_{123}\Delta\varepsilon_1 + c_{223}\Delta\varepsilon_2 + c_{233}\Delta\varepsilon_3 \\
C_{33} &= C_{33}^0 + c_{133}\Delta\varepsilon_1 + c_{233}\Delta\varepsilon_2 + c_{333}\Delta\varepsilon_3 \\
C_{44} &= C_{44}^0 + c_{144}\Delta\varepsilon_1 + c_{244}\Delta\varepsilon_2 + c_{344}\Delta\varepsilon_3 \\
C_{55} &= C_{55}^0 + c_{155}\Delta\varepsilon_1 + c_{255}\Delta\varepsilon_2 + c_{355}\Delta\varepsilon_3 \\
C_{66} &= C_{66}^0 + c_{166}\Delta\varepsilon_1 + c_{266}\Delta\varepsilon_2 + c_{366}\Delta\varepsilon_3 .
\end{aligned} \tag{2}$$

Transverse isotropic symmetry puts additional constrains on the tensor elements:

$$\begin{aligned}
c_{112} &= c_{111} - c_{166} - 3c_{266} \\
c_{122} &= c_{111} - 2c_{166} - 2c_{266} \\
c_{222} &= c_{111} + c_{166} - c_{266} \\
c_{223} &= c_{113} \\
c_{233} &= c_{133} \\
c_{123} &= c_{113} - 2c_{366} \\
c_{244} &= c_{155} = c_{144} + 2c_{456} \\
c_{255} &= c_{144} \\
c_{355} &= c_{344} .
\end{aligned} \tag{3}$$

In consequence, the number of parameters reduces to ten: $c_{111}, c_{113}, c_{133}, c_{144}, c_{166}, c_{266}, c_{333}, c_{344}, c_{366}$ and c_{456}. By assuming that the radial strains are equal ($\Delta\varepsilon_1 = \Delta\varepsilon_2$, due to equal stiffnesses and stress changes in the horizontal plane) we reduce equations (2) and (3) to:

$$\begin{aligned}
C_{11} &= C_{11}^0 + (2c_{111} - c_{166} - 3c_{266})\Delta\varepsilon_1 + c_{113}\Delta\varepsilon_3 \\
C_{13} &= C_{13}^0 + (2c_{113} - 2c_{366})\Delta\varepsilon_1 + c_{133}\Delta\varepsilon_3 \\
C_{33} &= C_{33}^0 + 2c_{133}\Delta\varepsilon_1 + c_{333}\Delta\varepsilon_3 \\
C_{44} &= C_{44}^0 + (2c_{144} + 2c_{456})\Delta\varepsilon_1 + c_{344}\Delta\varepsilon_3 \\
C_{66} &= C_{66}^0 + (c_{166} + c_{266})\Delta\varepsilon_1 + c_{366}\Delta\varepsilon_3 .
\end{aligned} \tag{4}$$

The assumption of isotropic radial strains results in additional constraints for the third-order elastic coefficients. This gives an opportunity to reparametrize the system in order to obtain a unique solution and limit the overall number of coefficients. First, the c_{144} and c_{456} coefficients are unique for C_{44}, and therefore can be substituted by:

$$c_{144}^* = 2c_{144} + 2c_{456}. \tag{5}$$

Furthermore, c_{111} is unique for C_{11}, and consequently c_{166} and c_{266} in C_{66} may be reparametrized, giving:

$$\begin{aligned}
c_{111}^* &= 2c_{111} - c_{166} - 3c_{266} \\
c_{166}^* &= c_{166} + c_{266} .
\end{aligned} \tag{6}$$

Consequently, the eight unique model parameters are: c_{111}^*, c_{113}, c_{133}, c_{144}^*, c_{166}^*, c_{333}, c_{344} and c_{366}. The reparametrized system of equations (4) is:

$$\begin{aligned}
C_{11} &= C_{11}^0 + c_{111}^*\Delta\varepsilon_1 + c_{113}\Delta\varepsilon_3 \\
C_{13} &= C_{13}^0 + 2(c_{113} - c_{366})\Delta\varepsilon_1 + c_{133}\Delta\varepsilon_3 \\
C_{33} &= C_{33}^0 + 2c_{133}\Delta\varepsilon_1 + c_{333}\Delta\varepsilon_3 \\
C_{44} &= C_{44}^0 + c_{144}^*\Delta\varepsilon_1 + c_{344}\Delta\varepsilon_3 \\
C_{66} &= C_{66}^0 + c_{166}^*\Delta\varepsilon_1 + c_{366}\Delta\varepsilon_3 .
\end{aligned} \tag{7}$$

It is worth noting that all the TOE tensor elements in equation (7), except for c_{144}^* and c_{344}, are influencing (directly or indirectly) more than one C_{ij}. Therefore, the determination of these TOE coefficients implies a joint inversion of all model elements (except for C_{44}).

3. EXPERIMENTAL DATA

For the purpose of this study we analyzed a field shale sample cored at 2750 meters true vertical depth in the North-Sea. Clay minerals content in the sample is approximately 75%. It has a porosity of 29% and a density of 2.23 g/cm^3 .

The experimental dataset, acquired in the SINTEF Formation Physics Laboratory, consists of records of axial and radial stresses and strains, pore pressure, temperature, and ultrasonic P- and S-wave travel times.

The measurements of ultrasonic P-wave travel times were carried out for several propagation angles, i.e. angles between the direction of wave propagation and the symmetry axis of the sample (bedding normal): 0° (axial, v_{Pz}), 37°, 47°, 68° and 90° (radial, v_{Pr}). The travel-times of the S-waves were measured along the axial and the radial directions (v_{Sz} and v_{Srr}).

The data were recorded under different stress paths (κ), i.e. different ratios between the radial and the axial stress changes (Eq. 8), around the expected in-situ stress.

$$\kappa = \frac{\Delta\sigma_{\mathrm{radial}}}{\Delta\sigma_{\mathrm{axial}}} . \tag{8}$$

Between every undrained loading-unloading cycle, there was a short drainage stage designed to change the pore pressure back to the expected true in-situ pore pressure. Figure 1 shows the time-development of the static and dynamic measurements during the experiment.

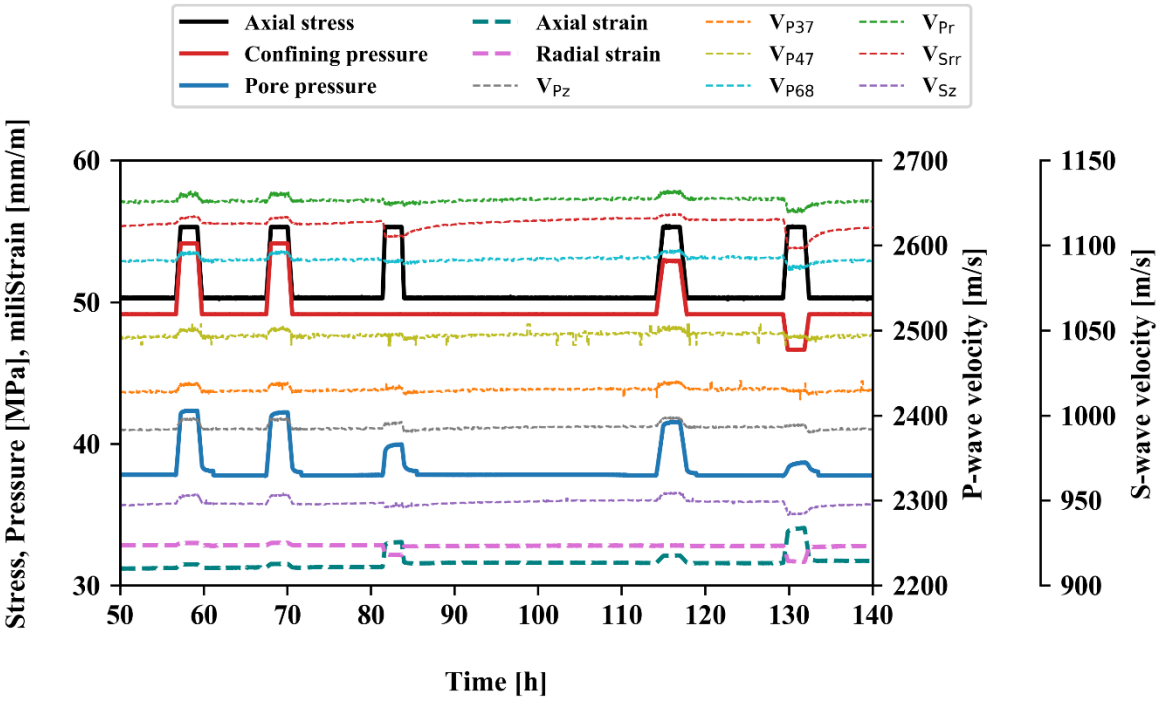

Figure 1. Laboratory test results (stresses, strains, pore pressure and ultrasonic velocities). The test consisted of two repeated hydrostatic cycles ($\kappa = \Delta\sigma_{radial}/\Delta\sigma_{axial} = 1$, stages 1-4, cf. Table 1), one triaxial cycle ($\kappa = 0$, stages 5 and 6), one K_0 cycle (no radial strain, here $\kappa \approx 0.75$, stages 7 and 8) and one constant mean stress (abbreviated as CMS, $\kappa = -0.5$, stages 9 and 10) loading-unloading cycle.

4. METHODOLOGY

In order to determine ultrasonic P- and S-wave velocities within the sample, we need to estimate travel times and combine them with information on sample dimensions given by initial sample length, radius and recorded strains. We use axial and radial velocities measured directly after the initial consolidation phase to estimate dynamic stiffness parameters C_{11}, C_{33}, C_{44} and C_{66}:

$$\begin{aligned} C_{11} &= v_{Pr}\rho \\ C_{33} &= v_{Pz}\rho \\ C_{44} &= v_{Sz}\rho \\ C_{66} &= v_{Srr}\rho \end{aligned}, \qquad (9)$$

where ρ is bulk density.

Estimation of C_{13} requires a different approach (Thomsen, 1986). Due to the small size of ultrasonic transducers we used in the experiment, we assume the oblique P-wave velocity measurements (at 37°, 47°, and 68°) to represent true group velocities. We have confirmed this assumption by numerical modelling. Consequently, we approximate C_{13} by fitting the estimated group velocities to the measured group velocities by minimization of root-mean-square (RMS) error. The phase velocity v_P at phase angle θ expressed by the elastic constants in a transversely isotropic medium is given by (Thomsen, 1986):

$$v_P(\theta) = \left(\frac{1}{2\rho}\left[C_{33} + C_{44} + (C_{11} - C_{33})\sin^2\theta + D(\theta)\right]\right)^{1/2}, \qquad (10)$$

where the $D^2(\theta)$ is defined as:

$$\begin{aligned} D^2(\theta) &= (C_{33} - C_{44})^2 \\ &+2\left[2(C_{13} + C_{44})^2 - (C_{33} - C_{44})(C_{11} + C_{33} - 2C_{44})\right] \\ &\sin^2\theta + \left[(C_{11} + C_{33} - 2C_{44})^2 - 4(C_{13} + C_{44})^2\right]\sin^4\theta. \end{aligned} \qquad (11)$$

The corresponding group angle ϕ becomes:

$$\phi(\theta) = \tan^{-1}\left(\left[\tan\theta + \frac{1}{v_P}\frac{dv_P}{d\theta}\right]\left[1 - \frac{\tan\theta}{V_P}\frac{dv_P}{d\theta}\right]^{-1}\right), \qquad (12)$$

and finally, the group velocity V_P is:

$$V_P^2(\phi) = v_P^2(\theta) + \left(\frac{dv_P}{d\theta}\right). \qquad (13)$$

An example of optimization of the fit of C_{13} to the experimental data is provided in Figure 2.

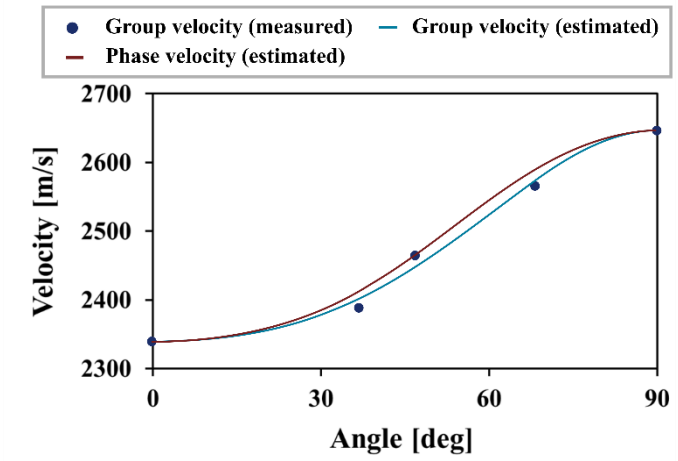

Figure 2. Example of C_{13} estimation plot and the relationship between group and phase velocity angular dependency. In this case, the estimated C_{13} = 7.0 GPa, or alternatively Thomsen's δ = 0.12.

To estimate the TOE tensor elements, for every undrained loading or unloading step we compare the reference stress state, just before the stress change, with the stressed state after the change. In both cases, we average over 20 data points at the end of the consolidation periods. For each of the points we estimate the reference stiffness C_{ij}^0 and the final stiffnesses C_{ij} with associated strains ε_k, and express them as stiffness and strain changes corresponding to the given loading or unloading stage. Then, we estimate the eight unique third-order elastic constants by numerically solving Eq. (4), i.e. optimizing the values of c_{ijk} tensor to minimize the RMS error between the modelled and the experimental C_{ij} matrix.

We can adjust the input to the available data. In order to have a (over-)determined system, we use at least two distinct stress cycles as input for the inversion of the eight unique TOE tensor elements. Generally, some of the expressions from Eq. (4) can be omitted in the inversion process (due to e.g. lack of input data), but once the expression for C_{13} is not used, the physical relationship between the elastic components of the model is lost. Therefore, even if the model predicts velocity changes with high accuracy, the elements of the TOE tensor should not be interpreted as medium's physical parameters.

5. RESULTS AND DISCUSSION

Results of the inversion for the TOE tensor are shown in Table 1. First, we inverted for c_{ijk} using data points from all available loading-unloading cycles (column "all κ"). Then we combined the third-order coefficients with recorded strains to obtain updated SOE matrix C_{ij} elements (Eq. (7)) and back-calculated velocity changes (Eq. (9) - (13)), shown in Figure 3.

Modelling of P- and S-wave velocity changes captured all general trends observed in the experimental data. Modelled radial P-wave velocities are slightly overestimated, whereas the modelled changes of vertical P-waves are generally too conservative (Figure 3, plot A), which is reflected in a relatively high RMS error.

Table 1. Summary of inversion for the full TOE tensor. The data have been divided according to input information used for inversion of c_{ijk} tensor (selection of stress paths, Eq. (8), i.e. loading/unloading stages used to estimate the TOE tensor): "all κ" – all available stress paths, all cycles except the repeated hydrostatic cycle (κ = 1, stages 3 and 4, cf. Figure 1), used as a reference case for further comparison; "κ = 1 & κ = 0.75" – hydrostatic and K_0, where $\kappa \approx 0.75$ gives $\Delta\varepsilon_r = 0$ for this shale; "κ = 0 & κ = -0.5" – triaxial and constant mean stress; and "κ = 1 & κ = -0.5" – hydrostatic and constant mean stress.

Stress paths κ [-]	all κ	κ = 1 & $\kappa \approx 0.75$	κ = 0 & κ = -0.5	κ = 1 & κ = -0.5
Stage no.	1,2, 5-10	1,2,7,8	5,6,9,10	1,2,9,10
$c_{ijk}[GPa]$				
c_{113}	130.4	146.4	165.0	114.7
c_{133}	104.6	49.1	103.0	114.9
c_{333}	127.4	232.4	122.1	129.1
c_{344}	31.6	34.8	46.7	28.3
c_{366}	26.3	51.9	61.2	8.9
c^*_{111}	388.8	291.4	468.4	360.4
c^*_{144}	88.6	71.7	122.8	82.7
c^*_{166}	111.4	24.1	191.1	74.8

In the case of S-waves (Figure 3, plot B), the development of vertical velocity changes is well recreated. However, radial S-wave modelling accuracy varies from one stress path to another – the modelled velocities are the most accurate for the hydrostatic and the K_0 stress paths.

The back-calculated (using inverted TOE tensor elements and strains) velocities of the oblique P-waves (Figure 3, plot C) fit the experimental data with high accuracy, both in terms of absolute velocity values prediction and velocity change trends reproduction. The modelling results managed to recreate gradual transition of P-wave behavior for the oblique angles (between the vertical and the radial direction) of propagation.

The RMS errors between modeled and measured P-wave velocities are shown in Table 2. For the P-waves, the misfit value is consistently low for all analyzed propagation directions except for the vertical v_{Pz}. This deficiency may be originating from relative values of the TOE tensor elements and relationships between them (Eq. (7)). In the case of C_{11}, i.e. the v_{Pr}, the largest

third-order tensor element (indicating largest impact of corresponding strain) is c^*_{111}, which is not constrained by any other SOE matrix component C_{ij}.

Table 2. RMS error between the modelled and measured velocities and stiffness parameters for different TOE tensor variants. The RMS errors are shown separately for all velocities ($v_{Pz}, v_{P37}, v_{P47}, v_{P68}, v_{Pr}, v_{Sz}, v_{Srr}$), averages for given modes ($v_{P,all}$, $v_{S,all}$), the average for all velocities (v_{all}) and average for all considered stiffness parameters ($C_{ij,all}$). The data have been divided according to input information used for inversion of c_{ijk} tensor (selection of stress paths, i.e. loading or unloading stages used to estimate the TOE tensor, cf. Figure 1).

Stress paths κ [-]	all κ	$\kappa = 1$ & $\kappa \approx 0.75$	$\kappa = 0$ & $\kappa = -0.5$	$\kappa = 1$ & $\kappa = -0.5$
Stage no.	1,2, 5-10	1,2,7,8	5,6,9,10	1,2,9,10
RMS fit error [m\s]				
v_{Pz}	3.79	19.48	3.90	3.55
v_{P37}	1.23	8.50	1.28	1.21
v_{P47}	1.37	5.51	2.03	1.36
v_{P68}	1.59	4.37	2.61	1.42
v_{Pr}	1.71	6.69	2.27	1.85
$v_{P,all}$	1.94	8.91	2.42	1.88
v_{Sz}	0.83	3.36	2.04	0.90
v_{Srr}	2.35	17.06	4.89	2.38
$v_{S,all}$	1.59	10.21	3.46	1.64
v_{all}	1.84	9.28	2.72	1.81
RMS fit error [GPa]				
$C_{ij,all}$	0.0227	0.0895	0.0277	0.0237

For C_{33}, the unconstrained third-order coefficient c_{333} is smaller than the associated coefficient ($2c_{133}$). The dominating parameter c_{133}, constrained by both C_{13} and C_{33}, is more affected by the inevitable presence of ultrasonic velocity estimation errors and inaccuracy of C_{13} approximation, which may explain the relatively high error of C_{33}, i.e. v_{Pz}, estimation.

In the case of the error in the S-wave velocities, the misfit differs significantly between the radial and vertical propagation direction. It may be caused by complete independence of the TOE tensor elements in the expression for C_{44} from the rest of the system of Eq. (7). This lack of additional constrains yields relatively good fit of modelled vertical S-wave velocity to the experimental values, but at the same time reduces our confidence in how accurately c^*_{144} and c_{344} values represent the actual physical medium parameters.

Our next step was to verify if we could obtain satisfactory modelling results using only a part of experimental data as the inversion input. We estimated c_{ijk} values using several sub-sets of stress paths and compared the resultant

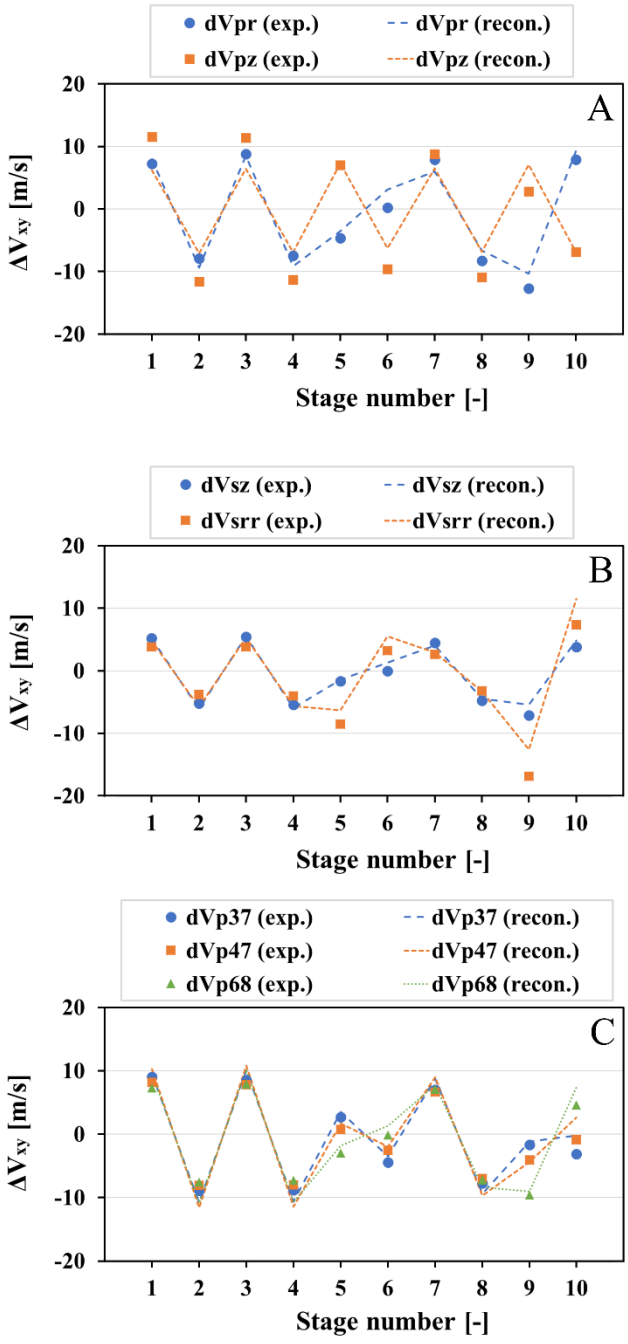

Figure 3. Comparison of experimentally measured ("exp.") and modelled ("recon.") ultrasonic velocity changes. Predictions of velocity changes were obtained with TOE tensor estimated using data from all stress paths (Table 1, column "all κ"). Plot A: P-waves, radial (dVpr) and vertical (dVpz). Plot B: S-waves, vertical (dVsz) and radial and horizontally-polarized (dVsrr). Plot C: P-wave, measured at 37° (dVp37), 47°(dVp47) and 68° (dVp68).

TOE parameters and velocity estimation errors to the previously described reference case based on the inversion of the entire data set.

The combination of input data from cycles following hydrostatic ($\kappa = 1$) and K_0 ($\kappa \approx 0.75$) stress paths yielded the largest discrepancies in TOE tensor element values, with an average difference between corresponding c_{ijk} parameters of 47% (compared to the reference TOE tensor), followed by triaxial ($\kappa = 0$) and constant mean stress (CMS, κ = -1/2) stress paths giving the average difference of 43%. The third-order coefficients set closest to the reference case was given by inversion of the data from the hydrostatic and the CMS stress paths ($\kappa = 1$ and -1/2, respectively), and its elements differed from the reference tensor on average by 18%.

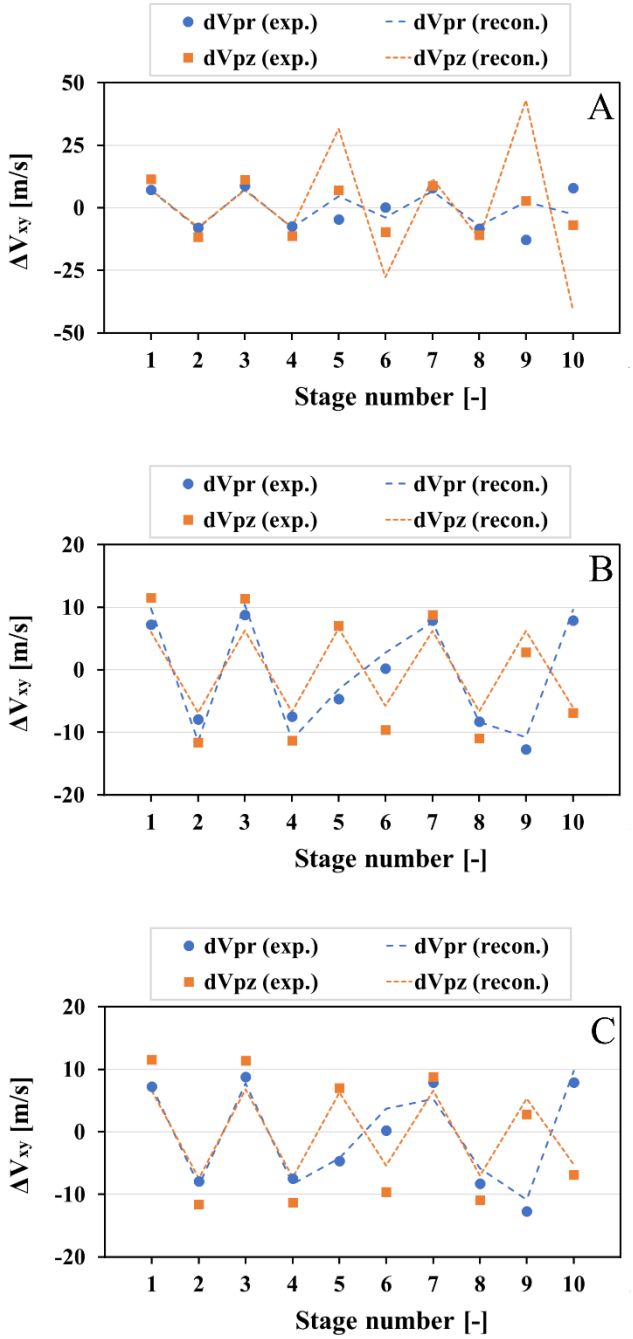

Figure 4. Comparison of experimentally measured ("exp.") and modelled ("recon.") ultrasonic vertical (dVpz) and radial (dVpr) P-wave velocity changes. Predictions of velocity changes were obtained with TOE tensor estimated using data from combinations of different loading-unloading cycles. Plot A: hydrostatic and K_0 stress paths (table 1, column "κ = 1 & κ = 0.75"). Plot B: triaxial and CMS stress paths column ("κ = 0 & κ = -0.5"). Plot C: hydrostatic and CMS stress paths ("κ = 1 & κ = -0.5").

However, it is worth noting that this variance is strongly affected by the discrepancy between values of c_{366} – one of the smallest elements of c_{ijk} tensor (i.e. does not have strong influence on stiffness strain-dependency).

Next, we used the c_{ijk} tensors obtained using only a part of experimental data to model velocity changes for all available loading or unloading stages, following the same procedure as in the reference case. The comparison of the different model realizations with the experimental data is shown in Figure 4 and Table 2.

The large differences between the values of the reference TOE tensor coefficients and the ones estimated from hydrostatic and K_0 stress cycles are also reflected in the general fit quality (Figure 4, plot A). Velocity changes are in good correspondence only for stress paths that were used in the inversion and are significantly overestimated for the triaxial and the CMS stress cycles. We observed the same type of misfit for S- and oblique P-waves. This observation is not surprising as the inverted stress paths (κ = 1 and $\kappa \approx 0.75$, respectively) are similar in nature, and differ significantly from the triaxial (κ = 0) and CMS (κ = -0.5) stress paths.

In the case of modelling using the TOE tensor determined from the triaxial and the CMS stress cycles, the difference between the corresponding TOE parameters and the reference parameters is not affecting the value of the velocity modelling error to the same extend as in the case in which for the inversion we used only the hydrostatic and K_0 stress paths. Although the data provides enough input characterized by relatively large strains to constrain the estimated stiffness changes, the average RMS error suggests that it still does not provide enough well-balanced information to optimize the TOE tensor elements (Figure 4, plot B).

The best overall velocity changes model was provided by the TOE tensor obtained from hydrostatic and constant mean stress cycles (Figure 4, plot C). On average, the accuracy of velocity modelling in this case is even slightly better than in the reference case. This is possible because c_{ijk} tensor was optimized using stiffnesses, not velocities. The two stress paths, representing the opposite extremes of the tested deformations spectrum, allow to obtain the TOE tensor not so different from the reference TOE parameters. This suggests that a large separation of

stress paths (κ) used as input in the inversion may be suitable for interpolation of the measured deformation range and give better results than extrapolation by using two neighboring stress paths. Therefore, we may argue that in a case when the intermediate stress paths data are not available, using extreme stress paths yields a decent approximation of the actual physical tensor and gives satisfactory estimates of the dynamic stiffness.

Finally, we used our dataset to compare the model we defined in Eq. (7) with a non-linearly elastic model proposed by Prioul et al., 2004. This model was derived under assumption of implicit isotropy of the TOE tensor, which allowed to limit the number of independent model parameters to three ($c_{111}^{\mathrm{iso}}, c_{112}^{\mathrm{iso}}$ and c_{123}^{iso}). If we assume equal radial strains, the model is defined as:

$$\begin{aligned}
C_{11} &= C_{11}^{0} + \left(c_{111}^{\mathrm{iso}} + c_{112}^{\mathrm{iso}}\right)\Delta\varepsilon_1 + c_{112}^{\mathrm{iso}}\Delta\varepsilon_3 \\
C_{13} &= C_{13}^{0} + \left(c_{112}^{\mathrm{iso}} + c_{123}^{\mathrm{iso}}\right)\Delta\varepsilon_1 + c_{112}^{\mathrm{iso}}\Delta\varepsilon_3 \\
C_{33} &= C_{33}^{0} + 2c_{112}^{\mathrm{iso}}\Delta\varepsilon_1 + c_{111}^{\mathrm{iso}}\Delta\varepsilon_3 \\
C_{44} &= C_{44}^{0} + \tfrac{1}{4}\left(c_{111}^{\mathrm{iso}} + c_{112}^{\mathrm{iso}} - 2c_{123}^{\mathrm{iso}}\right)\Delta\varepsilon_1 \\
&\quad + \tfrac{1}{4}\left(c_{111}^{\mathrm{iso}} - c_{112}^{\mathrm{iso}}\right)\Delta\varepsilon_3 \\
C_{66} &= C_{66}^{0} + \tfrac{1}{2}\left(c_{111}^{\mathrm{iso}} - c_{112}^{\mathrm{iso}}\right)\Delta\varepsilon_1 + \tfrac{1}{2}\left(c_{112}^{\mathrm{iso}} - c_{123}^{\mathrm{iso}}\right)\Delta\varepsilon_3 .
\end{aligned} \tag{14}$$

In order to compare the isotropic TOE tensor (Prioul et. Al, 2004) with the anisotropic reference tensor (Fuck and Tsvankin, 2009), we estimated the c_{ijk}^{iso} elements using data from all stress paths as input for the tensor inversion (as in the reference case). Next, we back-calculated velocity changes and estimated modelling error following the same procedure as in the previous examples (see Table 3.).

Table 3. The isotropic third-order elastic tensor c_{ijk}^{iso} (Prioul, et al., 2004) estimated using measured strains and stiffnesses from all available stress paths (top) and the corresponding averages of RMS error of velocity modelling: for axial, radial and oblique P-waves ($v_{P,all}$), axial and radial S-waves ($v_{S,all}$), global average for all measured waves (v_{all}, bottom) and global average for all considered stiffness coefficients ($C_{ij,all}$). Average RMS errors can be directly compared with values shown in column "all κ" in Table 2.

c_{ijk}^{iso} [GPa]			
c_{111}^{iso}	c_{112}^{iso}	c_{123}^{iso}	
133.6	92.4	96.6	
RMS fit error			
$v_{\mathrm{P,all}}$ [m\s]	$v_{\mathrm{S,all}}$ [m\s]	v_{all} [m\s]	$C_{ij,\mathrm{all}}$ [GPa]
4.10	5.03	4.37	0.0366

The comparison of vertical and radial velocities predicted by the two models is shown in Figure 5 (plots A and B, respectively). In the case of vertical P-wave (v_{Pz}), for which the isotropic TOE tensor gives RMS error of 4.62 m/s, both models achieve similar velocity prediction accuracy. For vertical S-wave (v_{Sz}), the isotropic model fails to reproduce the velocities correctly, and for triaxial and CMS stress paths (stages 5, 6, 9 and 10) fails to predict the direction of velocity changes. For radial P- and S-waves, the c_{ijk}^{iso} produces velocity changes roughly following the trends observed in the laboratory data, but significantly less accurate than in the anisotropic reference case. The oblique P-wave velocity estimates obtained with the use of the anisotropic model exhibit similarly better fit to experimental data in comparison to the isotropic model. This difference in modelling accuracy is reflected in the relatively high average RMS error values, as shown in Table 3.

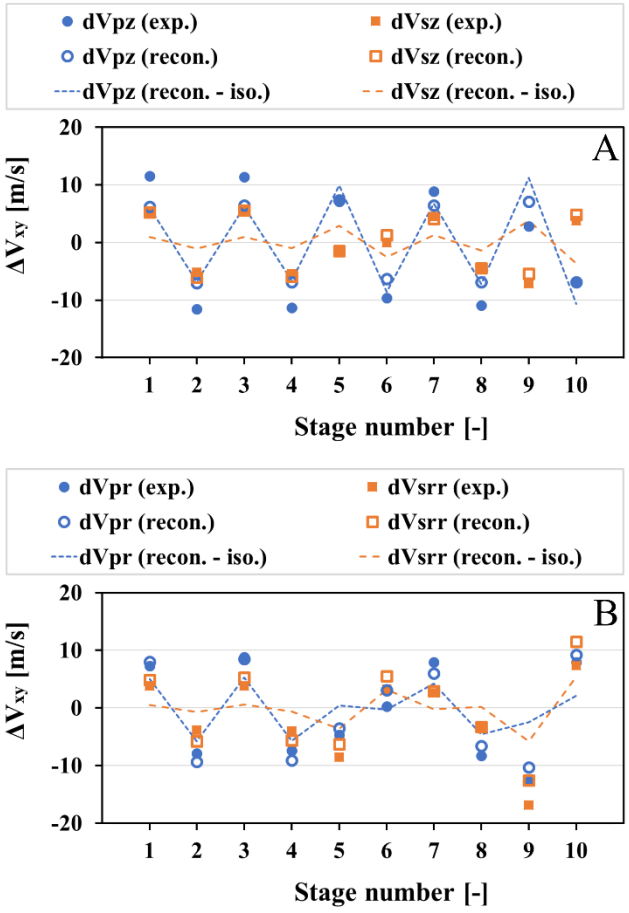

Figure 5. Comparison of velocity changes modelled with the anisotropic third-order elastic tensor under assumption of transverse isotropy of stiffnesses, stresses and strains ("recon.") and the third-order elastic tensor derived with assumption of its implicit isotropy ("recon. – iso.", Prioul et al., 2004) with velocity changes estimated directly from laboratory measurements ("exp."). Plot A: vertical P- (dVpz) and S-wave (dVsz). Plot B: radial P- (dVpr) and radial and horizontally polarized S-wave (dVsrr).

6. CONCLUSIONS

With the use of the anisotropic third-order elastic (TOE) tensor for hexagonal symmetry proposed by Fuck and Tsvankin, 2009, we derived a strain-dependent velocity model for transversely isotropic shales for the case of horizontally isotropic stress changes and strains.

The model employs a set of eight independent parameters obtained by numerical inversion of laboratory data. Our dataset consists of statically measured axial and radial strains and changes of the five VTI medium stiffness matrix (C_{ij}) elements estimated from dynamic measurements of ultrasonic velocities.

The resultant TOE tensor allowed to back-calculate ultrasonic velocity changes directly from strains with high accuracy and to correctly recreate trends observed in the experimental data.

We confirmed the predictive power of the model by inverting for the TOE parameters using only a limited portion of the laboratory data and using the resultant tensor to successfully recreate experimentally observed velocity changes in the entire dataset.

We found that the velocity fitting quality depends strongly on the extent and on the choice of sub-set of the experimental data used for the inversion. We compared three different model realizations based on the TOE tensors obtained by inverting only two out of four available stress paths (ratio of horizontal and vertical stress changes, κ). The TOE tensor closest to the reference tensor (obtained by inversion of all available loading-unloading cycles) and providing the best ultrasonic velocity fit was obtained by inverting the data taken from stress cycles differing significantly in deformation character (hydrostatic and CMS stress paths, κ = 1 and κ = - 0.5, respectively). Therefore, we conclude that if no data from the intermediate stress paths are available, the extreme stress paths may be used to approximate the actual physical TOE tensor and the dynamic stiffness.

We compared the velocity change prediction accuracy of the anisotropic model with a simplified non-linearly elastic model assuming implicit isotropy of the third-order elastic tensor (Prioul et al., 2004). The comparison shows that anisotropic strain sensitivity is required to adequately estimate velocity changes in intrinsically anisotropic sedimentary rocks, such as shales.

To further deepen our analysis, more shales need to be examined. This may reveal trends and correlations between the TOE parameters and other petrophysical properties.

ACKNOWLEDGEMENTS

This publication has been produced with support from the NCCS Centre, performed under the Norwegian research program Centres for Environment-friendly Energy Research (FME); and the Knowledge-building Projects for Industry under the Norwegian Research Council: “Shale rock physics: Improved seismic monitoring for increased recovery” and “Improved prediction of stress and pore pressure changes in the overburden for infill drilling”. The authors acknowledge the following partners for their contributions: Aker Solutions, ANSALDO Energia, CoorsTek Membrane Sciences, EMGS, Gassco, KROHNE, Larvik Shipping, Norcem, Norwegian Oil and Gas, Quad Geometrics, Shell, Equinor, TOTAL, and the Research Council of Norway (257579/E20); AkerBP, Engie, INEOS, and Total (234074/E30); and AkerBP, Equinor, and Shell (294369/E30).

REFERENCES

1. Bachrach, R. and P. Avseth. 2008. Rock physics modeling of unconsolidated sands: Accounting for nonuniform contacts and heterogeneous stress fields in the effective media approximation with applications to hydrocarbon exploration. *Geophysics*, 73, E197-E209.
2. Budiansky, B. and R.J. O'Connell. 1976. Elastic moduli of a cracked solid. *International Journal of Solids and Structures*, 12, 81-97.
3. Fjær, E. 2006. Modeling the stress dependence of elastic wave velocities in soft rocks. *ARMA/USRMS,* 06-1070.
4. Fjær, E., R.M. Holt, P. Horsrud, , A. M. Raaen, and R. Risnes. 2008. *Petroleum related rock mechanics. Developments in Petroleum Science*, 53.
5. Fuck, R.F., A. Bakulin, and I. Tsvankin. 2009. Theory of traveltime shifts around compacting reservoirs: 3D solutions for heterogeneous anisotropic media. *Geophysics*, 74, D25-D36.
6. Fuck, R.F. and I. Tsvankin. 2009. Analysis of the symmetry of a stressed medium using nonlinear elasticity. *Geophysics*, 74, WB79-WB87.
7. Hudson, J.A. 1981. Wave speeds and attenuation of elastic waves in material containing cracks. *Geophysical Journal International*, 64, 133-150.
8. Johnson, P.A. and P.N.J. Rasolofosaon. 1996. Nonlinear elasticity and stress-induced anisotropy in rock. *Journal of Geophysical Research: Solid Earth*, 101, 3113-3124.
9. Mindlin, R.D. 1949. Compliance of elastic bodies in contact. *Journal of Applied Mechanics*, 16, 259-268.
10. Prioul, R., A. Bakulin, and V. Bakulin. 2004. Nonlinear rock physics model for estimation of 3D subsurface stress in anisotropic formations: Theory and laboratory verification. *Geophysics*, 69, 415-425.
11. Thomsen, L. 1986. Weak Elastic Anisotropy. *Geophysics*, 51, 1954-1966.
12. Walton, K. 1987. The effective elastic moduli of a random packing of spheres. *Journal of the Mechanics and Physics of Solids*, 35, 213-226.